



# Decoration of cobalt/iron oxide nanoparticles on N-doped carbon nanosheets: Electrochemical performances for lithium-ion batteries

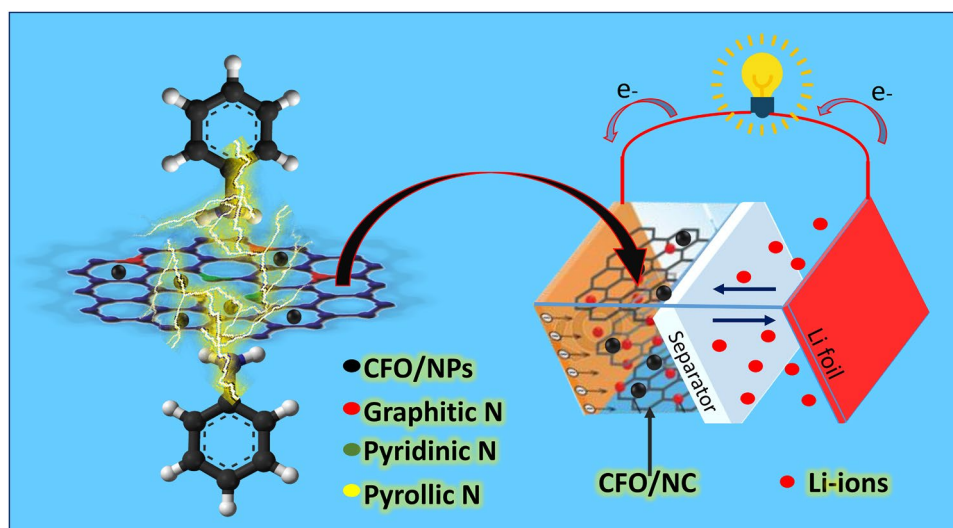
Muhammad Kashif Aslam<sup>1</sup> · Syed Shoaib Ahmad Shah<sup>2</sup> · Tayyaba Najam<sup>2</sup> · Sha Li<sup>1</sup> · ChangGuo Chen<sup>1</sup>

Received: 22 November 2018 / Accepted: 22 January 2019 / Published online: 9 February 2019  
© Springer Nature B.V. 2019

## Abstract

Cobalt/iron oxide nanoparticles (CFO/NPs) were fabricated with a facile solid combustion method and decorated on polyaniline-derived porous N-doped carbon nanosheets. The N-doped carbon nanosheets provide a pathway for charge transfer and act as defensive layers to avoid the agglomeration of nanoparticles. The decoration of CFO nanoparticles on porous N-doped carbon nanosheets (CFO/NC) typically leads to hybrid material that displays an exceptionally high electrochemical performance for Li-ion batteries (LIBs) with excellent diffusion of electrolyte ions and ensures fast  $\text{Li}^+/\text{e}^-$  transport. The initial discharge capacity reaches up to  $1270 \text{ mAh g}^{-1}$  ( $1.65 \text{ mAh cm}^{-2}$ ) at a current density of  $500 \text{ mA g}^{-1}$  ( $0.65 \text{ mA cm}^{-2}$ ). Furthermore, it also exhibits an exceptionally high specific capacity of  $635 \text{ mAh g}^{-1}$  at a high current density of  $500 \text{ mA g}^{-1}$  ( $500 \text{ mA g}^{-1}$ ) after long cycling (250 cycles) and a remarkable rate capability with 93% capacity retention. These excellent electrochemical characteristics demonstrate that CFO/NC is a promising anode material for LIBs.

## Graphical abstract



**Keywords** Binary oxide · N-doped carbon nanosheet · Anode material · Lithium-ion battery

✉ Muhammad Kashif Aslam  
aslam\_kashif@outlook.com

✉ ChangGuo Chen  
cgchen@cqu.edu.cn

Extended author information available on the last page of the article

## 1 Introduction

Lithium-ion batteries (LIBs) are currently one of the most widely used rechargeable energy storage systems in portable devices. However, the small lithium storage and poor cycling stability are still major issues of new/novel materials which

limit their commercialization. Better energy storage materials with high efficiencies and long lives are required for portable devices and electricity storage for wind and solar power [1–4]. To fulfill the market demands, researchers are therefore identifying novel materials for electrodes with high specific capacities and good cycling stabilities. Moreover, the limited capacity of commercial graphite (anode material for LIB) [5, 6] and safety issues prompted the search for alternative anode materials.

Various conversion-typed binary metal oxides, such as  $\text{CuCo}_2\text{O}_4$  [7],  $\text{ZnCo}_2\text{O}_4$  [8],  $\text{NiCo}_2\text{O}_4$  [9],  $\text{FeCo}_2\text{O}_4$  [10],  $\text{CoFe}_2\text{O}_4$  (CFO) [11],  $\text{CoMn}_2\text{O}_4$  [12],  $\text{Co}_2\text{SnO}_4$  [13], and  $\text{Co}_3\text{O}_4$  [14], are considered to be the most promising candidates. Among all oxides, CFO is extensively studied as anode material because of its promising theoretical capacity ( $916 \text{ mAh g}^{-1}$ ). However, the stable cycling performance with high capacity is unsatisfactory (Table 1). Therefore, the performance of CFO has been improved using a composite approach based on conductive materials such as graphene and carbon nanotubes [15]. Recently, much attention has been paid to doping techniques and the morphology [16–18]. Electrically conductive N-doped carbon (NC) materials have been achieved through the calcination of different precursors, which in turn protects the metals from corrosion and aggregation during electrochemical reactions [19, 20]. The controlled calcination of polyaniline nanosheets is beneficial for the exploitation of porous NC materials [21–23]. More importantly, the synergy between metal oxides and the NC lattice creates sufficient localized reactive sites by modifying the charge distribution on the carbon surface via electron transfer promotion.

In this study, we decorate  $\text{CoFe}_2\text{O}_4$  nanoparticles (CFO/NPs) on porous N-doped carbon (PNC) nanosheets by post-synthetic sonication for further use as anodic LIB material. Polymer carbonization is a relatively convenient method for the synthesis of PNC and can be extended for the large-scale fabrication of nanomaterials. As a result, the CFO/NC anode exhibits a highly reversible capacity, high rate capability, and excellent cyclic stability ( $635 \text{ mAh g}^{-1}$  reversible capacity after 250 cycles at a current density of  $500 \text{ mA g}^{-1}$ ). The excellent Li-ion storage performance of CFO/NC is attributed to the unique nanostructure and the synergistic effect of CFO/NC.

## 2 Experimental

### 2.1 Synthesis of CFO/NPs

Typically,  $\text{FeCl}_2 \cdot 4\text{H}_2\text{O}$  (5 mmol, Aldrich) and  $\text{Co}(\text{OH})_2$  (2.5 mmol; Aldrich) were separately dissolved in 50 ml  $\text{HNO}_3$  (Merck). These solutions were mixed at  $80 \text{ }^\circ\text{C}$  for  $\sim 2 \text{ h}$  under constant stirring. Urea (6 mmol, Fluka

Chemika) was added to the solution and heated to  $100 \text{ }^\circ\text{C}$  for 13 h to evaporate the water. The dried product was grounded to fine powder with a ball milling machine (high-energy ball mill  $E_{\text{max}}$ ) and annealed at  $700 \text{ }^\circ\text{C}$  in air for 6 h at a heating rate of  $3 \text{ }^\circ\text{C min}^{-1}$  to obtain CFO/NPs. Urea acts as fuel, and nitrate ions are used as oxidizers. Fine spinel oxides were the products and  $\text{N}_2$ ,  $\text{H}_2\text{O}$ , and  $\text{CO}_2$  were the gases evolved. A systematic scheme of the preparation method is shown in Fig. 1.

### 2.2 Synthesis of NC nanosheets

For the synthesis of NC nanosheets, 4 g of aniline was dissolved in 400 ml of 0.5 M  $\text{H}_2\text{SO}_4$ . Subsequently, 8.75 g of ammonium per sulfate (APS) was dissolved in 50 ml of water, added to the above-mentioned solution, and the mix was stirred for 24 h at  $4 \text{ }^\circ\text{C}$ . The obtained product was washed several times. A systematic scheme of the preparation method is shown in Fig. 1. The polyaniline was further carbonized at  $900 \text{ }^\circ\text{C}$  for 2 h in a  $\text{N}_2$  atmosphere to obtain PNC nanosheets.

### 2.3 Synthesis of CFO/NC

For the synthesis of the CFO/NC composite, the NC nanosheets and CFO/NPs were mixed with a 1:4 mass ratio, respectively. Firstly, the NC sheets were dispersed in 20 ml of deionized water under sonication for 30 min. Subsequently, CFO/NPs were added and the solution was further sonicated for 1 h.

### 2.4 Materials characterization

The crystalline structure of as prepared was characterized by X-ray diffraction (XRD, X'PertProPHILIPsx-ray diffractometer) with  $\text{Cu K}\alpha$  radiations  $\lambda = 1.54184 \text{ \AA}$ . Fourier transform infrared spectroscopy (FT-IR). Raman spectra and FT-IR spectrum studies were also performed to check the carbon structure and purity of the material, respectively. The surface morphology was analyzed by field emission electron microscopy (FESEM, JEOL JSM-7800F). High-resolution transmission electron microscopy (HRTEM) was performed on a JEOL-2100F microscope at 200 kV. The valence oxidation state of different elements' atoms were determined by using X-rays photoelectron spectroscopy (XPS, ESCALAB250 analyzer, and Al  $\text{K}\alpha$  radiation). Textural properties of the CFO/NC were determined by Brunauer–Emmett–Teller (BET, at  $77.3 \text{ K}$  with a Quanta chrome NOVA-4200e system).

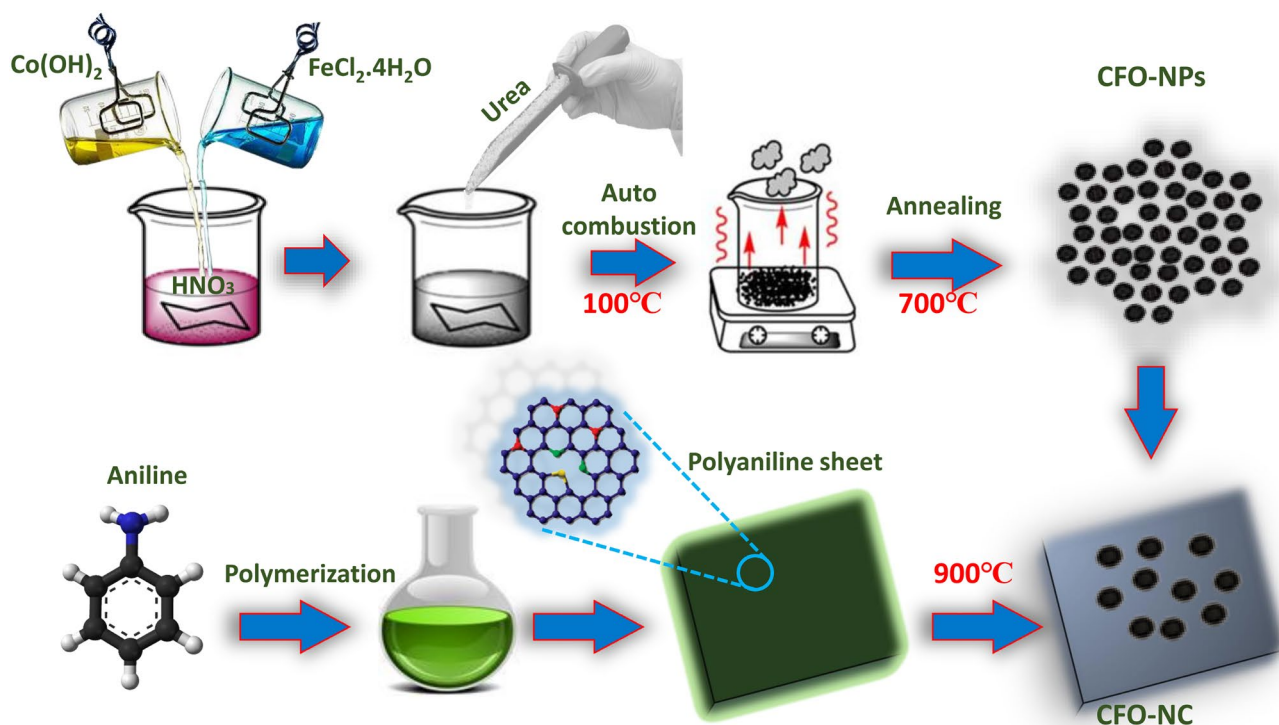


Fig. 1 Schematic illustration of synthesis of CFO/NPs, NC nanosheets, and CFO/NC

## 2.5 Electrochemical measurements

To test the electrochemical properties of the prepared CFO/NC, coin cells (CR2032) were assembled in an inert atmosphere in an argon gas-filled glove box. A slurry containing active materials, SP-carbon, and PVDF binder at a ratio of 80:10:10 was used to assemble the coin cells. The slurry was prepared in *N*-methyl-2-pyrrolidone (NMP) solvent and stirred for 8 h to ensure complete homogeneity. The slurry was applied to the copper (Cu) foil as current collector and dried at 60 °C for 12 h under vacuum. The coated Cu foil was pressed under 5–10 MP pressure with a roller and cut into circular discs (diameter = 7 mm). The mass of the active material on each electrode ranged between 1 and 1.2 mg cm<sup>-2</sup>. Lithium foil was used as counter and reference electrode. The 1M LiPF<sub>6</sub> was used as electrolyte and was dissolved in DMC/EMC/EC at a ratio of 1:1:1 by volume. A polypropylene microporous polyethylene (PE) membrane film (Celgard 2400) was used as separator. The whole cell was assembled in a glove box filled with pure Ar gas (oxygen and water contents below 1 ppm). All cells were aged for the percolation of the electrolyte before the electrochemical measurements. The charge–discharge cycle profiles were determined with a Neware battery testing system (model 5V—5 mA) in the potential window of 0.01–3 V versus Li<sup>+</sup>/Li. Cyclic voltammetry (CV) was performed at a scan rate of 0.2 mV s<sup>-1</sup> in the potential window

of 0.01–3 V (CHI 660E, CH Instruments, China). Electrochemical impedance spectroscopy (EIS) was performed at 0.01 Hz–100 kHz; the first open circuit potential (OCV) was measured. The EIS data were collected with a workstation (CHI 660E, CH Instruments, China).

## 3 Results and discussion

The CFO/NPs were synthesized by modifying a previously reported method [24] and PNC nanosheets were prepared by carbonization of polyaniline (Fig. 1). The CFO/NPs and NC nanosheets were used to prepare a CoFe<sub>2</sub>O<sub>4</sub>/NC composite (CFO/NC) using a post-synthetic approach. The phase purity was confirmed by XRD. Figure 3a shows the XRD patterns of CFO/NPs, NC, and CFO/NC. All peaks were indexed as (220), (311), (400), (511), and (440) planes of the spinel phase in CFO/NPs (JCPDS card no. 22-1086), which confirms the high purity of the synthesized CFO/NPs. The XRD pattern of NC exhibits a broad peak at 24.5°, which is attributed to the crystallinity of carbon. The XRD pattern of CFO/NC also exhibits a carbon peak at 24.6° (Fig. 3a), which provides robust evidence for the combination of CFO/NC and NC nanosheets. The field emission electron microscopy (FESEM) images (Fig. 2a, d) of CFO/NPs confirm the homogeneous spherical morphology of CFO/NPs with average diameters of 80–100 nm. The FESEM images of CFO/



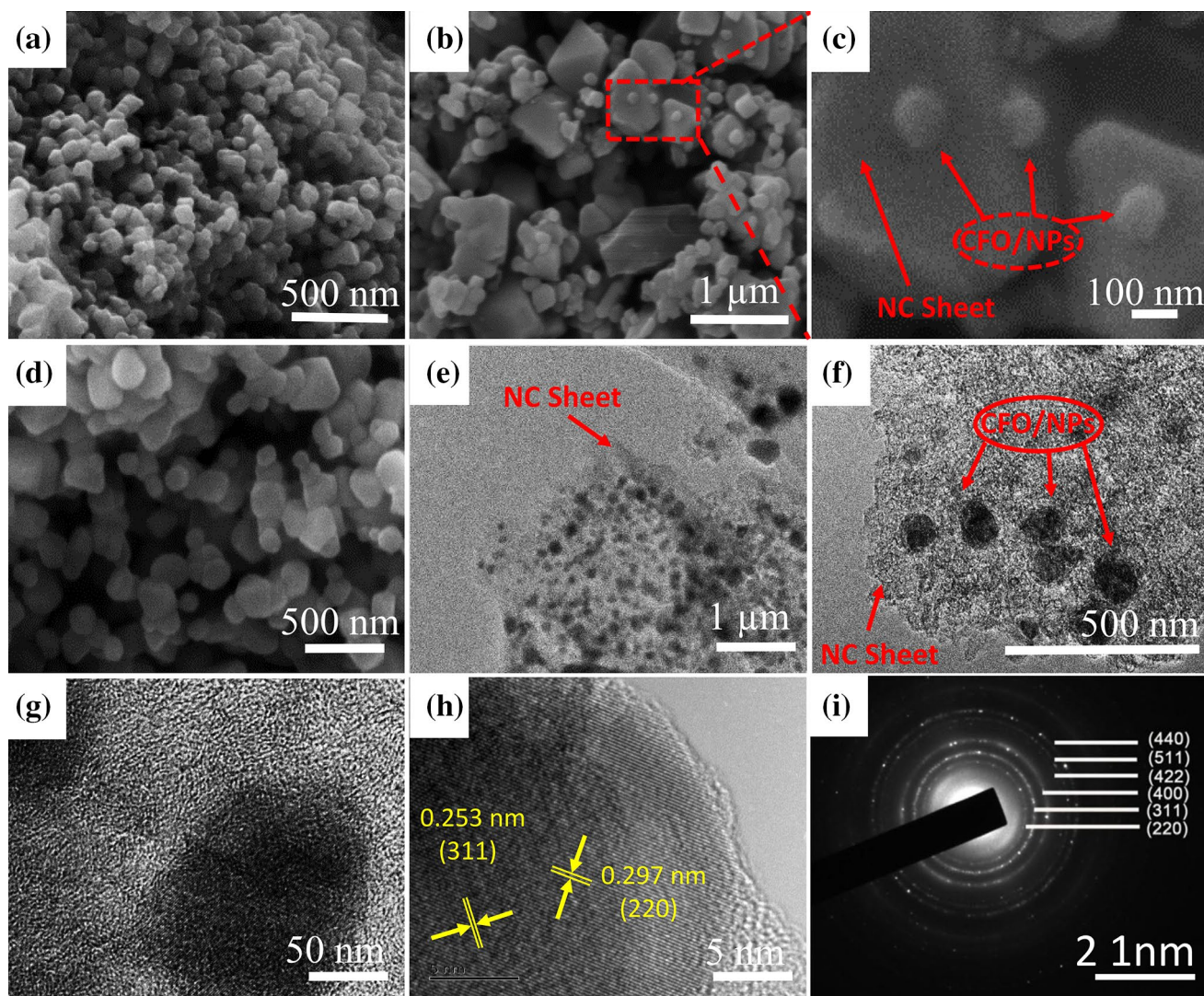


**Fig. 2** FESEM images of as-prepared CFO/NPs (a, d) and CFO/NC (b, c), TEM images of CFO/NC at low (e, f) and high (g, h) magnification, SAED image of CFO/NPs (i)

NC further confirm the decoration of CFO nanoparticles on PNC nanosheets (Fig. 2b, c). To illustrate the formation of CFO/NPs and CFO/NC, high-resolution transmission electron microscopic (HRTEM) studies were also performed. Figure 2e–g clearly shows the decoration of CFO/NPs on PNC-sheet, and Fig. 2h reveals the lattice fringes with interplanar spacings of 0.297 nm and 0.253 nm corresponds to the (220) and (311) lattice planes of CFO/NPs, respectively. The selected area electron diffraction (SAED) pattern of CFO/NPs shows well-defined concentric rings, which can be assigned to the lattice planes of CFO/NPs as shown in Fig. 2i, which is consistent with XRD results. The formation of CFO/NPs was also confirmed with FT-IR spectroscopy (Fig. 3b). The vibrational features between 500 and 600  $\text{cm}^{-1}$  are due to the intrinsic stretching vibrations at tetrahedral sites and the band between 350 and 450  $\text{cm}^{-1}$  is

caused by stretching vibrations at octahedral sites. Furthermore, the bands at 461 and 584  $\text{cm}^{-1}$  in the CFO/NP product correspond to Co–O and Fe–O bonds, respectively. The vibrational features at 1118 and 1631  $\text{cm}^{-1}$  are attributed to C–O stretching [25] and that at 3433  $\text{cm}^{-1}$  (broad stretching vibration of O–H) indicates the presence of water molecules adsorbed on the surface of the material.

Figure 3c shows the Raman spectra of the CFO/NC materials, which can be used to further investigate the carbon structure. The calculated  $I_D/I_G$  ratio between the D- and G-bands is 0.84, indicating the presence of graphitic carbon in the active material. This is beneficial for achieving better electronic conduction between adjacent NPs; it improves the electrochemical performance.

Furthermore, the electronic structure and elemental composition of CFO/NC were investigated by XPS. The XPS

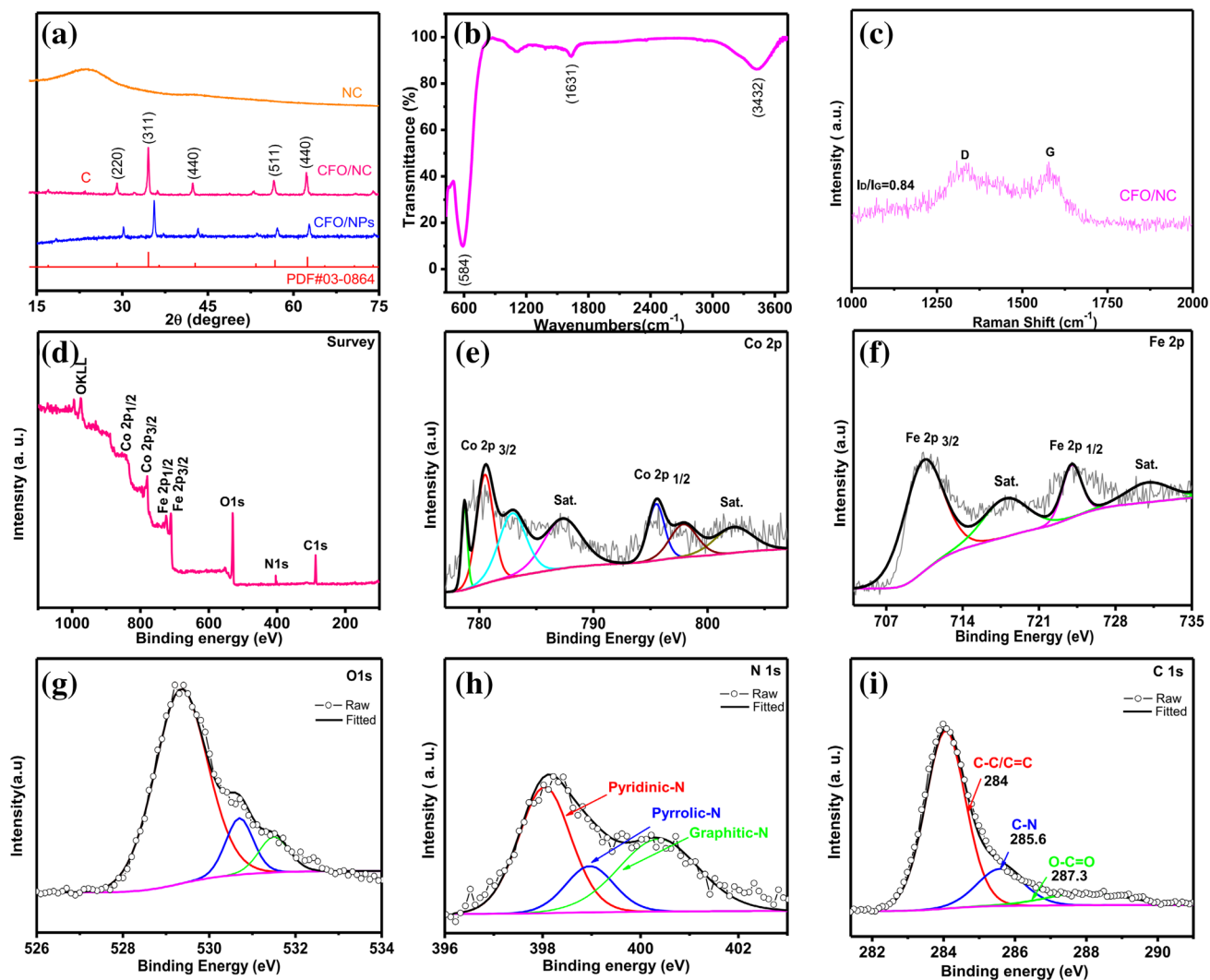


**Fig. 3** **a** XRD patterns of as-prepared CFO/NPs, NC nanosheets, and CFO/NC, **b** FT-IR spectrum of CFO/NPs, **c** Raman spectrum of CFO/NC, **d** survey XPS of CFO/NC and its high-resolution XPS of Co2p (**e**), Fe2p (**f**), O 1s (**g**), N 1s (**h**), C 1s (**i**)

(Fig. 3d) clearly indicates the presence of Co, Fe, O, N, and C in CFO/NC, which supports the results obtained from XRD, FT-IR, and Raman analyses. The high-resolution XPS of Fe 2p (Fig. 3e) exhibits two main peaks at the binding energies of 710.5 and 723.9 eV and two weak satellite peaks (denoted as Sat.) at 718.4 and 733.7 eV corresponding to Fe 2p<sub>3/2</sub> and Fe 2p<sub>1/2</sub>, respectively. These spin–orbit peaks of Fe 2p<sub>3/2</sub> and Fe 2p<sub>1/2</sub> are attributed to the presence of Fe<sup>3+</sup> [16]. Figure 3f shows the XPS spectrum of the Co 2p core level, which contains two major peaks at 780.4 and 795.6 eV that are related to Co 2p<sub>3/2</sub> and Co 2p<sub>1/2</sub>. The satellite peaks at binding energies of 787.7 eV and 803.2 eV are two shakeup-type peaks of Co in the high binding energy state of the Co 2p<sub>3/2</sub> and Co 2p<sub>1/2</sub> edges, which demonstrate the presence of Co<sup>2+</sup> in the sample. The spin–orbit splitting between the two strong signals is 15.2 eV, which suggests

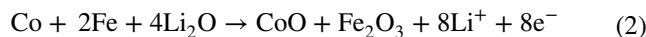
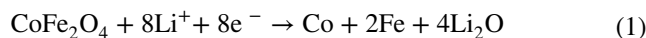
that Co<sup>2+</sup> and Co<sup>3+</sup> coexist in the CFO/NC. The broad peak at 529.4 eV (Fig. 3g) in the high-resolution XPS of O1s is due to the metal–oxygen bond [26] and the peaks at 530.7 and 531.6 eV can be attributed to C–O and O–H, respectively [26]. The deconvoluted peaks in the high-resolution spectrum of N 1s (Fig. 3h) include three peaks of pyridinic N (35.3%), graphitic N (37.4%), and pyrrolic N (26.9%) species [27]. Pyridinic N enhances the surface wettability [28, 29], while graphitic N improves diffusion-limited properties [29, 30]. The high-resolution spectrum of C 1s (Fig. 3i) also presents peaks of C–C/C=C (76.39%), C–N (17.33%), and O–C=O (6.27%) species. Hence, these XPS results show that CFO/NC with its own mixing composition including Fe<sup>3+</sup>, Co<sup>2+</sup>, and O<sup>2-</sup>, confirmed the formation of CFO/NC and are in good promise with XPS results. The surface area and pore size distribution were further investigated

via nitrogen adsorption–desorption isotherms of CFO/NC (Fig. 4). The BET surface area of CFO/NC is  $23 \text{ m}^2 \text{ g}^{-1}$ , which is higher than that previously reported for binary metal oxides such as porous octahedral  $\text{CoFe}_2\text{O}_4$  ( $7.6 \text{ m}^2 \text{ g}^{-1}$ ) [14] and  $\text{Co}_3\text{O}_4/\text{CoFe}_2\text{O}_4$  nanocomposites ( $7 \text{ m}^2 \text{ g}^{-1}$ ) [31]. This high surface area is attributed to highly porous NC. It is known that the larger the surface area is, the greater are the channels and locations for fast intercalation/deintercalation of  $\text{Li}^+$  ions into the host electrode material. The considerably high surface area of the CFO/NC electrode also has a dominant effect on good electrochemical performance and cycling stability due to the small diffusion length for  $\text{Li}^+$  ions and electrons and a greater number of electrolyte ions in the inner matrix space of the electrode.

### 3.1 Electrochemical performances

The prepared materials (CFO/NC, CFO, and NC) were further tested as anode materials for Li-ion batteries. The CV curves of the CFO/NC electrode recorded at a scan rate of  $0.2 \text{ mV s}^{-1}$  are shown in Fig. 5c. During the first discharge cycle of the CFO/NC electrode, a strong reduction peak in cathodic scan [32] is observed at  $\sim 0.46 \text{ V}$ , which is in agreement with the reduction of  $\text{Co}^{2+}$  and  $\text{Fe}^{3+}$  to their metallic states due to the formation of  $\text{Li}_2\text{O}$ , as illustrated in Eq. (1), accompanied by electrolyte decomposition into a solid interphase (SEI) layer. During the first anodic [33] charge process of the CFO/NC electrode, only one anodic peak ( $1.69 \text{ V}$ ) can

be attributed to the oxidation of metallic Co and Fe, which is illustrated in Eq. (2).



However, the binary metal oxide stores Li during the reversible formation and breakdown of  $\text{Li}_2\text{O}$ . During the cycling, only one cathodic and anodic peak is observed, which agrees with the reduction of  $\text{Fe}^{3+}$  and  $\text{Co}^{2+}$  merging into one peak [34]. The cathodic peaks in the second cycle of the CFO/NC electrode are slightly shifted to a higher potential of  $0.93 \text{ V}$ , which could be related to the reduction of  $\text{Fe}^{3+}$  and  $\text{Co}^{2+}$  ions, while the anodic peaks remain at the same potentials and overlap during each cycle, indicating that the capacity does not decrease after cycling. Notably, the integrated peak area and intensity during the cathodic and anodic polarization process remain the same after the first cycle, revealing a good electrochemical performance, reversibility, and cycling stability of the CFO/NC electrodes. The CV curves of the CFO/NPs and NC nanosheets are shown in Fig. 5. The CV curves of CFO/NPs show a severe intensity decrease of the oxidation peaks and shift to a higher potential, indicating severe capacity loss and polarization [34]. The charge–discharge profile of nanostructured CFO/NC was measured at a current density of  $500 \text{ mA g}^{-1}$  in the potential window from  $0.01$  to  $3.00 \text{ V}$ . The discharge capacity of the first cycle is  $1270 \text{ mAh g}^{-1}$ , which is much higher than the theoretical capacity of  $916 \text{ mAh g}^{-1}$ . This excellent

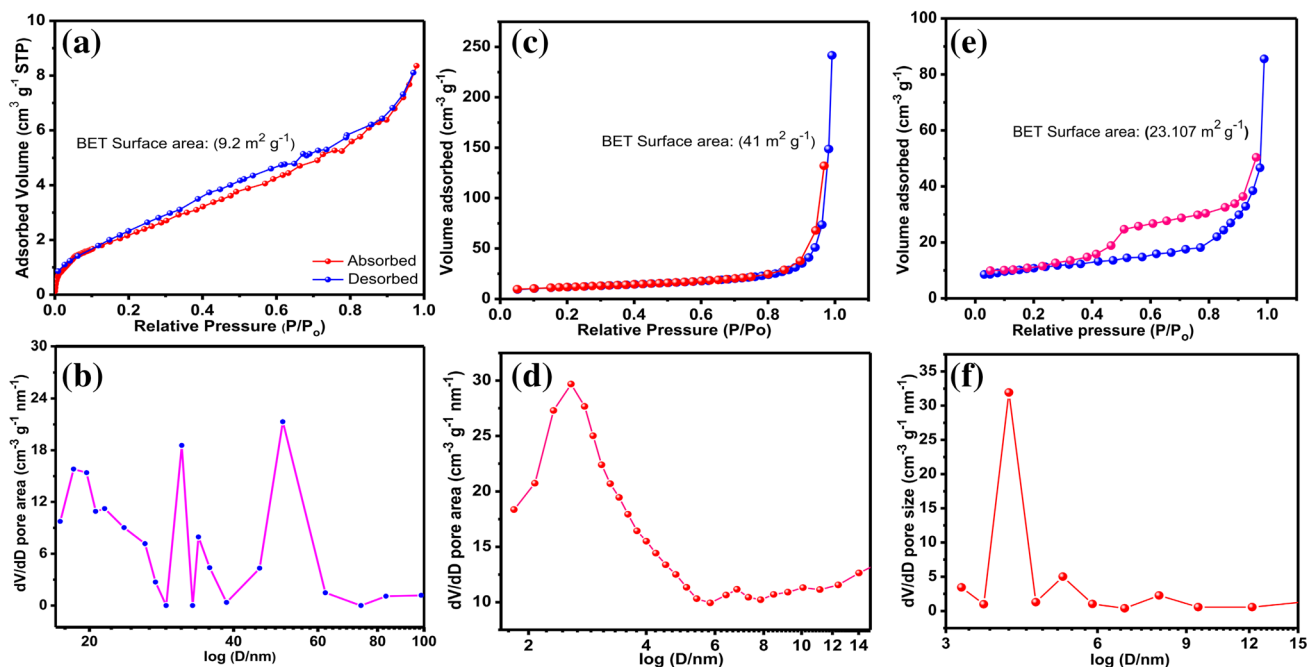


**Fig. 4** The BET-specific surface area and pore size of CFO/NPs (a, b), NC nanosheets (c, d), and CFO/NC (e, f)



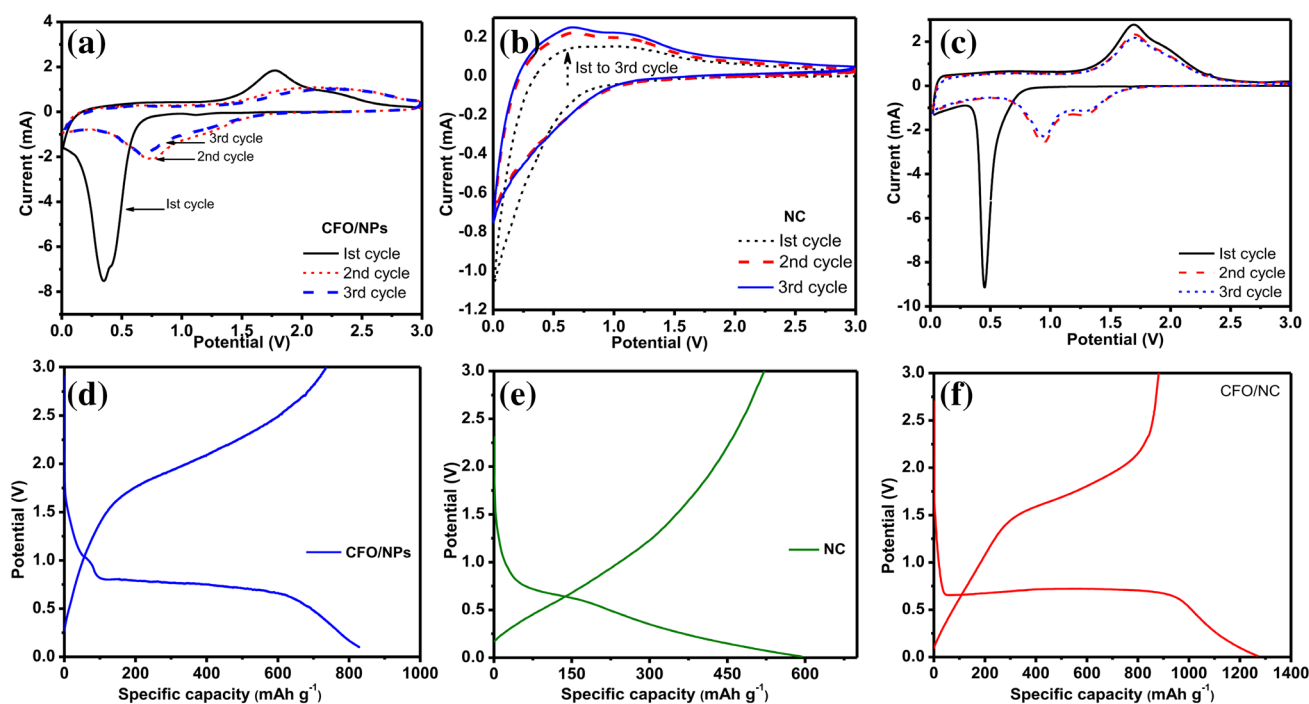


**Fig. 5** CV curves and first charge–discharge profiles of CFO/NPs (a, d), NC Nanosheets (b, e), and CFO/NC (c, f)

electrochemical performance is due to the typical decoration of CFONPs on NC nanosheets, chemical composition, high surface area, and pore size. The PNC nanosheets have an increased conductivity and create a pathway for fast Li-ion transport. The potential plateaus can be observed in the first discharge profile (Fig. 5d). In the first discharge profile, the potential quickly decays, which first leads to a plateau at  $\sim 0.66$  V which corresponds to a capacity of  $950 \text{ mAh g}^{-1}$ . Subsequently, a smooth and gradual slope can be observed up to  $0.01$  V; this plateau is absent in all the following cycles. This is because the initial discharges of  $\text{Co}^{2+}$  and  $\text{Fe}^{3+}$  have different electrochemical potentials versus Li; however, after deep discharge to  $0.01$  V, nano-domains of metallic Fe and Co NPs are formed [35], which will not transform back to CFO during the following cycles. The charge–discharge profiles of CFO/NPs and NC are also shown in Fig. 5. In the later discharge profiles, a very small capacity decay is observed in the initial 50 cycles. Thereafter, the cycling performance stabilizes and capacity loss is not observed. The charge–discharge performance of the CFO/NC electrode at a constant current density of  $500 \text{ mA g}^{-1}$  is shown in Fig. 6a. After long cycling (250 cycles), the discharge capacity is  $635 \text{ mAh g}^{-1}$ , which reveals very good cycling stability and insignificant capacity loss. Moreover, the electrochemical charge and discharge capacities of each cycle match very well during long cycling, indicating good cycling with  $\sim 100\%$  coulombic efficiency. Figure 6b shows the rate capabilities of CFO/NC, CFO/NPs, and NC nanosheet electrodes

at various current densities from  $100$  to  $1500 \text{ mA g}^{-1}$ . The average discharge capacities of CFO/NC are  $\sim 1095$ ,  $821$ ,  $674$ ,  $491$ , and  $296 \text{ mAh g}^{-1}$  at current densities of  $100$ ,  $200$ ,  $400$ ,  $800$ , and  $1500 \text{ mA g}^{-1}$ , respectively. When the current density returns to  $100 \text{ mA g}^{-1}$ , the CFO/NC electrode still has a  $93\%$  reversible capacity, demonstrating its excellent reversibility. The CFO/NPs have a  $40\%$  capacity, which is much smaller than that of the CFO/NC electrode. Figure 7a shows the charge–discharge profiles of CFO/NC at different cycle numbers. Figure 7b shows the charge–discharge profiles at different current densities. Table 1 shows the comparison of the electrochemical performance between CFO/NC and previously reported CFO-based materials with different structures and morphologies. It manifests that the CFO/NC prepared by polymerization exhibits an excellent cycle performance and high rate capacity, which is attributed to its chemical composition, especially to PNC, and the high surface area. It is a good anode material for LIBs. To further justify the excellent electrochemical performance, high reversibility, and excellent rate capability, EIS was carried out. The Nyquist plots of CFO/NPs, NC sheets, and CFO/NC before cycling are shown in Fig. 7c. All plots show a depressed semi-circle in the high-frequency region, which is related to the charge transfer resistance ( $R_{ct}$ ) of the electrode, and an inclined line at low frequency, corresponding to the Warburg diffusion process ( $Z_w$ ). The intersection of the semi-circle with the real axis in the high-frequency region (denoted as  $R_s$ ) is correlated to the internal resistance. The

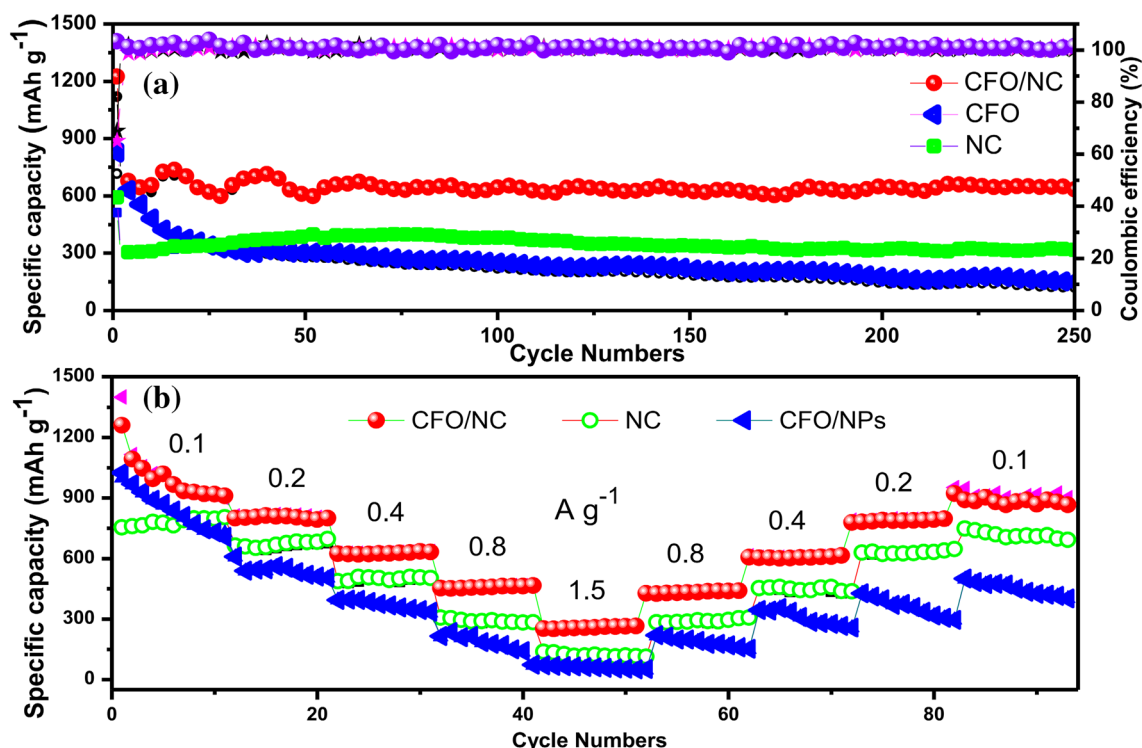


**Fig. 6** The long cycling charge–discharge performance of all the electrodes (a) and rate capabilities of all the electrodes at different current densities (b)

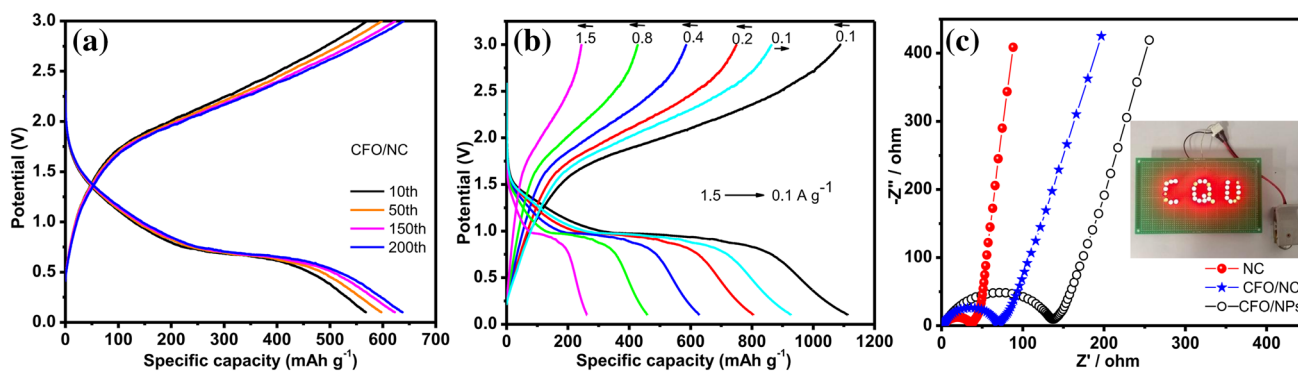


**Fig. 7** The charge–discharge profiles of different cycles at a current density of  $500 \text{ mA g}^{-1}$  (a), charge–discharge profiles at different current densities (b). The EIS Nyquist plots of all as-prepared electrodes (c) (inset; LED emitting light)

$R_{ct}$  value calculated for the CFO/NC electrode before cycling is  $70 \Omega$ . It is evidently much smaller than the value for CFO/NPs ( $136 \Omega$ ). The decrease in  $R_{ct}$  of the CFO/NC electrode can be attributed to the unique decoration of CFO/NP structures; combined with residual amorphous NC nanosheets, it is favorable for the delocalization of electrons and ions [36, 37].

To estimate the electrochemical performance of the prepared CFO/NC electrode, coin cells (CR2032) were fabricated using Li foil as the counter electrode. The CFO/NC electrode

stably powers 32 red light-emitting diodes (LEDs; inset of Fig. 7c), which demonstrates that the coin cell with the CFO/NC composite as anode material can be applied in practice.

## 4 Conclusion

We synthesized NC nanosheets decorated with CFO/NPs using a facile strategy, which can be developed for large-scale fabrication. The obtained CFO/NC composite can be



**Table 1** Comparison of the electrochemical performance between CFO/NC and other previously reported CFO-based materials with different structures and morphologies

Active materials	Observed discharge (Disch) and charge (Charg) capacities at various cycles, ( $\pm 5$ ) mAh g <sup>-1</sup>					References
	1st charge	1st discharge	2nd charge	2nd discharge	Current density (mA g <sup>-1</sup> )	
Mesoporous CoFe <sub>2</sub> O <sub>4</sub>	612	850	520	550	200	[38]
CoFe <sub>2</sub> O <sub>4</sub> /carbon fiber	1116	1398	1115	1190	200	[39]
Co <sub>3</sub> O <sub>4</sub> /CoFe <sub>2</sub> O <sub>4</sub>	1053	1314	950	1040	200	[14]
C@ CoFe <sub>2</sub> O <sub>4</sub> mesoporous	605	971	580	620	100	[40]
CoFe <sub>2</sub> O <sub>4</sub> /C nanofiber	720	1076	708	705	100	[41]
CoFe <sub>2</sub> O <sub>4</sub> octahedral	990	1179	970	975	200	[31]
CoFe <sub>2</sub> O <sub>4</sub> Flower like	995	1354	920	930	70	[42]
CFO/NC	1054	1270	708	714	500	This work

used as anode for Li-ion batteries. It shows an excellent initial discharge capacity of 1270 mAh g<sup>-1</sup> at a current density of 500 mA g<sup>-1</sup>. At a high current density of 500 mA g<sup>-1</sup>, it exhibits a capacity of 635 mAh g<sup>-1</sup> after 250 cycles. The active phase and synergy between metal oxides and NC nanosheets greatly improve the specific capacity, cycling stability, and rate capabilities. The present work demonstrates that NC nanosheets derived from polyaniline polymer have a synergistic effect on the electrochemical performance.

**Acknowledgements** This work is supported by National Natural Science Foundation of China (Grant No. 21273292).

## References

- Goodenough JB, Park K-S (2013) The Li-Ion rechargeable battery: a perspective. *J Am Chem Soc* 135:1167–1176
- Panwar NL, Kaushik S, C, Kothari S (2011) Role of renewable energy sources in environmental protection: a review. *Renew Sustain Energy Rev* 15:1513–1524
- Li J, Aslam MK, Chen C (2018) One-pot hydrothermal synthesis of porous  $\alpha$ -Ni(OH)<sub>2</sub>/C composites and its application in Ni/Zn alkaline rechargeable battery. *J Electrochem Soc* 165:A910–A917
- Li S, Cen Y, Xiang Q, Aslam MK, Hu B, Li W, Tang Y, Yu Q, Liu Y, Chen C (2019) Vanadium dioxide-reduced graphene oxide binary host as an efficient polysulfide plague for high-performance lithium-sulfur batteries. *J Mater Chem A*. <https://doi.org/10.1039/C8TA10422K>
- Zhou Y, Liu Y, Zhao W, Wang H, Li B, Zhou X, Shen H (2015) Controlled synthesis of series Ni<sub>x</sub>Co<sub>3-x</sub>O<sub>4</sub> products: morphological evolution towards quasi-single-crystal structure for high-performance and stable lithium-ion batteries. *Sci Rep* 5:11584
- Huang G, Zhang F, Zhang L, Du X, Wang J, Wang L (2014) Hierarchical NiFe<sub>2</sub>O<sub>4</sub>/Fe<sub>2</sub>O<sub>3</sub> nanotubes derived from metal organic frameworks for superior lithium ion battery anodes. *J Mater Chem A* 2:8048–8053
- Sun S, Wen Z, Jin J, Cui Y, Lu Y (2013) Synthesis of ordered mesoporous CuCo<sub>2</sub>O<sub>4</sub> with different textures as anode material for lithium ion battery. *Microporous Mesoporous Mater* 169:242–247
- Song X, Ru Q, Zhang B, Hu S, An B (2014) Flake-by-flake ZnCo<sub>2</sub>O<sub>4</sub> as a high capacity anode material for lithium-ion battery. *J Alloys Compd* 585:518–522
- Zheng F, Zhu D, Chen Q (2014) Facile fabrication of porous Ni<sub>x</sub>Co<sub>3-x</sub>O<sub>4</sub> nanosheets with enhanced electrochemical performance as anode materials for Li-ion batteries. *ACS Appl Mater Interfaces* 6:9256–9264
- Mohamed SG, Chen C-J, Chen CK, Hu S-F, Liu R-S (2014) High-performance lithium-ion battery and symmetric supercapacitors based on FeCo<sub>2</sub>O<sub>4</sub> nanoflakes electrodes. *ACS Appl Mater Interfaces* 6:22701–22708
- Guo H, Li T, Chen W, Liu L, Yang X, Wang Y, Guo Y (2014) General design of hollow porous CoFe<sub>2</sub>O<sub>4</sub> nanocubes from metal-organic frameworks with extraordinary lithium storage. *Nanoscale* 6:15168–15174
- Yang G, Xu X, Yan W, Yang H, Ding S (2014) Single-spinneret electrospinning fabrication of CoMn<sub>2</sub>O<sub>4</sub> hollow nanofibers with excellent performance in lithium-ion batteries. *Electrochim Acta* 137:462–469
- Zhang J, Liang J, Zhu Y, Wei D, Fan L, Qian Y (2014) Synthesis of Co<sub>2</sub>SnO<sub>4</sub> hollow cubes encapsulated in graphene as high capacity anode materials for lithium-ion batteries. *J Mater Chem A* 2:2728–2734
- Fu X, Chen D, Wang M, Yang Y, Wu Q, Ma J, Zhao X (2014) Synthesis of porous CoFe<sub>2</sub>O<sub>4</sub> octahedral structures and studies on electrochemical Li storage behavior. *Electrochim Acta* 116:164–169
- Aslam MK, Shah SSA, Li S, Chen C (2018) Kinetically controlled synthesis of MOF nanostructures: single-holed hollow core-shell ZnCoS@Co<sub>9</sub>S<sub>8</sub>/NC for ultra-high performance lithium-ion batteries. *J Mater Chem A* 6:14083–14090
- Yang X, Wang X, Zhang Z (2005) Electrochemical properties of submicron cobalt ferrite spinel through a co-precipitation method. *J Cryst Growth* 277:467–470
- Lavela P, Tirado JL (2007) CoFe<sub>2</sub>O<sub>4</sub> and NiFe<sub>2</sub>O<sub>4</sub> synthesized by sol-gel procedures for their use as anode materials for Li ion batteries. *J Power Sources* 172:379–387
- Ding Y, Yang Y, Shao H (2012) Synthesis and characterization of nanostructured CuFe<sub>2</sub>O<sub>4</sub> anode material for lithium ion battery. *Solid State Ionics* 217:27–33
- Torad NL, Salunkhe RR, Li Y, Hamoudi H, Imura M, Sakka Y, Hu C-C, Yamauchi Y (2014) Electric double-layer capacitors based on highly graphitized nanoporous carbons derived from ZIF-67. *Chem Eur J* 20:7895–7900
- Liu Y, Jiang H, Zhu Y, Yang X, Li C (2016) Transition metals (Fe, Co, and Ni) encapsulated in nitrogen-doped carbon nanotubes

- as bi-functional catalysts for oxygen electrode reactions. *J Mater Chem A* 4:1694–1701
21. Liu B, Shioyama H, Akita T, Xu Q (2008) Metal-organic framework as a template for porous carbon synthesis. *J Am Chem Soc* 130:5390–5391
  22. Sun J-K, Xu Q (2014) Functional materials derived from open framework templates/precursors: synthesis and applications. *Energy Environ Sci* 7:2071–2100
  23. Bhattacharyya S, Konkena B, Jayaramulu K, Schuhmann W, Maji TK (2017) Synthesis of nano-porous carbon and nitrogen doped carbon dots from an anionic MOF: a trace cobalt metal residue in carbon dots promotes electrocatalytic ORR activity. *J Mater Chem A* 5:13573–13580
  24. Liu J, Xiao J, Zeng X, Dong P, Zhao J, Zhang Y, Li X (2017) Combustion synthesized macroporous structure MFe<sub>2</sub>O<sub>4</sub> (M = Zn, Co) as anode materials with excellent electrochemical performance for lithium ion batteries. *J Alloys Compd* 699:401–407
  25. Sharifi I, Shokrollahi H, Doroodmand MM, Safi R (2012) Magnetic and structural studies on CoFe<sub>2</sub>O<sub>4</sub> nanoparticles synthesized by co-precipitation, normal micelles and reverse micelles methods. *J Magn Magn Mater* 324:1854–1861
  26. Marco JF, Gancedo JR, Gracia M, Gautier JL, Ríos E, Berry FJ (2000) Characterization of the nickel cobaltite, NiCo<sub>2</sub>O<sub>4</sub>, prepared by several methods: an XRD, XANES, EXAFS, and XPS study. *J Solid State Chem* 153:74–81
  27. Xia W, Mahmood A, Zou R, Xu Q (2015) Metal-organic frameworks and their derived nanostructures for electrochemical energy storage and conversion. *Energy Environ Sci* 8:1837–1866
  28. Tang C, Wang H-F, Chen X, Li B-Q, Hou T-Z, Zhang B, Zhang Q, Titirici M-M, Wei F (2016) Topological defects in metal-free nanocarbon for oxygen electrocatalysis. *Adv Mater* 28:6845–6851
  29. Liu Y, Shen Y, Sun L, Li J, Liu C, Ren W, Li F, Gao L, Chen J, Liu F, Sun Y, Tang N, Cheng H-M, Du Y (2016) Elemental superdoping of graphene and carbon nanotubes. *Nat Commun* 7:10921
  30. Amiin IS, Liu X, Pu Z, Li W, Li Q, Zhang J, Tang H, Zhang H, Mu S (2018) From 3D ZIF nanocrystals to Co–Nx/C nanorod array electrocatalysts for ORR, OER, and Zn–Air batteries. *Adv Funct Mater* 28:1704638
  31. Rai AK, Gim J, Thi TV, Ahn D, Cho SJ, Kim J (2014) High rate capability and long cycle stability of Co<sub>3</sub>O<sub>4</sub>/CoFe<sub>2</sub>O<sub>4</sub> nanocomposite as an anode material for high-performance secondary lithium ion batteries. *J Phys Chem C* 118:11234–11243
  32. Shi W, Zhu J, Rui X, Cao X, Chen C, Zhang H, Hng HH, Yan Q (2012) Controlled synthesis of carbon-coated cobalt sulfide nanostructures in oil phase with enhanced Li storage performances. *ACS Appl Mater Interfaces* 4:2999–3006
  33. Wang Y, Wu J, Tang Y, Lü X, Yang C, Qin M, Huang F, Li X, Zhang X (2012) Phase-controlled synthesis of cobalt sulfides for lithium ion batteries. *ACS Appl Mater Interfaces* 4:4246–4250
  34. Xing Z, Ju Z, Yang J, Xu H, Qian Y (2013) One-step solid state reaction to selectively fabricate cubic and tetragonal CuFe<sub>2</sub>O<sub>4</sub> anode material for high power lithium ion batteries. *Electrochim Acta* 102:51–57
  35. Mao J, Hou X, Wang X, Hu S, Xiang L (2015) The cubic aggregated CoFe<sub>2</sub>O<sub>4</sub> nanoparticle anode material for lithium ion battery with good performance. *Mater Lett* 161:652–655
  36. Xie Q, Li F, Guo H, Wang L, Chen Y, Yue G, Peng D-L (2013) Template-free synthesis of amorphous double-shelled zinc–cobalt citrate hollow microspheres and their transformation to crystalline ZnCo<sub>2</sub>O<sub>4</sub> microspheres. *ACS Appl Mater Interfaces* 5:5508–5517
  37. Xie Q, Zeng D, Ma Y, Lin L, Wang L, Peng D-L (2015) Synthesis of ZnO–ZnCo<sub>2</sub>O<sub>4</sub> hybrid hollow microspheres with excellent lithium storage properties. *Electrochim Acta* 169:283–290
  38. Duan L, Wang Y, Wang L, Zhang F, Wang L (2015) Mesoporous MFe<sub>2</sub>O<sub>4</sub> (M = Mn, Co, and Ni) for anode materials of lithium-ion batteries: synthesis and electrochemical properties. *Mater Res Bull* 61:195–200
  39. Wang B, Li S, Wu X, Li B, Liu J, Yu M (2015) Nanocrystal-constructed mesoporous CoFe<sub>2</sub>O<sub>4</sub> nanowire arrays aligned on flexible carbon fabric as integrated anodes with enhanced lithium storage properties. *Phys Chem Chem Phys* 17:21476–21484
  40. Wang J, Yang G, Wang L, Yan W, Wei W (2017) C@CoFe<sub>2</sub>O<sub>4</sub> fiber-in-tube mesoporous nanostructure: formation mechanism and high electrochemical performance as an anode for lithium-ion batteries. *J Alloys Compd* 693:110–117
  41. Zhou J, Yang T, Mao M, Ren W, Li Q (2015) Enhanced electrochemical performance of hierarchical CoFe<sub>2</sub>O<sub>4</sub>/MnO<sub>2</sub>/C nanotubes as anode materials for lithium-ion batteries. *J Mater Chem A* 3:12328–12333
  42. Xiong QQ, Tu JP, Shi SJ, Liu XY, Wang XL, Gu CD (2014) Ascorbic acid-assisted synthesis of cobalt ferrite (CoFe<sub>2</sub>O<sub>4</sub>) hierarchical flower-like microspheres with enhanced lithium storage properties. *J Power Sources* 256:153–159

**Publisher's Note** Springer Nature remains neutral with regard to jurisdictional claims in published maps and institutional affiliations.

## Affiliations

Muhammad Kashif Aslam<sup>1</sup>  · Syed Shoaib Ahmad Shah<sup>2</sup> · Tayyaba Najam<sup>2</sup> · Sha Li<sup>1</sup> · ChangGuo Chen<sup>1</sup>

<sup>1</sup> College of Chemistry and Chemical Engineering, Chongqing University, Chongqing 401331, People's Republic of China

<sup>2</sup> Department of Chemistry, The Islamia University of Bahawalpur, Bahawalpur 63100, Pakistan